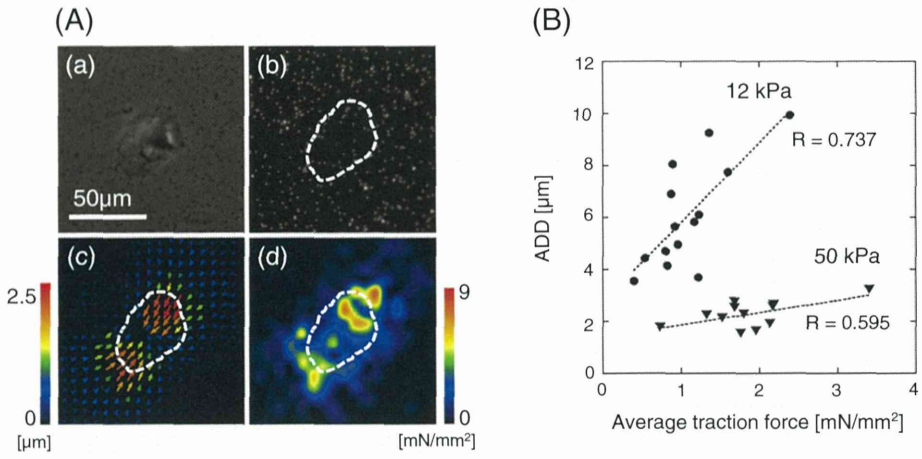

Fig. 2. (A) Parts (a) and (b) show the phase-contrast and fluorescent images of the hiPS-CM and the substrate with fluorescence beads (1 μm diameter), respectively. Part (c) is an example of a displacement field image of fluorescence beads calculated by the particle image velocimetry (PIV) algorithm. Part (d) shows an example of a traction force field image calculated using the PIV result from part (c) by the Fourier transform traction cytometry (FTTC) method. (B) Correlation between ADD and the normalized traction force (at 12 kPa (●) and 50 kPa (▼)) estimated with the FTTC algorithm. Bar in (a) represent 50 μm. The color scales for (c) and (d) are as indicated beside each of the figures.

decreased or almost momentarily stopped at the point of the negative deflection in the FP (see also Supplementary Movies 1 and 2). In the presence of 100 nM E-4031, there was a major decrease in the contractile parameters, MCS, MRS, ADD and the beating rate (Fig. 6E–G).

3.3.3. The effects of a Ca^{2+} channel blocker, verapamil

Fig. 7A shows the alterations in the motion and FP profiles of the hiPS-CMs in accordance with the verapamil concentration (0, 90, 150 nM). Increasing the verapamil concentration caused a progressive decrease in both the FPD and CRD that was well correlated with the correlation coefficient (R = 0.970) (Fig. 7B). The slope of the linear regression was found to be 0.633 (FPD/CRD). Since verapamil has an L-type Ca^{2+}-channel inhibiting effect, increasing verapamil concentration led to a decrease in FP_{slow} (Fig. 7A). Addition of verapamil also caused MCS to become smaller. There was a good correlation between the amplitudes of FP_{slow} and MCS, when these parameters were evaluated as a percent of the control, with a correlation coefficient of 0.921 (Fig. 7C). Increasing verapamil concentration also caused the MRS as well as ADD to decrease (Fig. 7C and D), and the beating rate to increase (Fig. 7E).

3.3.4. The effects of the positive inotropic reagent, isoproterenol

Fig. 8A shows the simultaneously measured motion and FP profile at isoproterenol concentrations of 0, 1, and 10 μM. With increasing isoproterenol concentrations, the CRD and FPD progressively shortened (Fig. 8A), with a good correlation observed (R = 0.943) (Fig. 8B). The slope of the linear regression was found to be 0.737 (FPD/CRD). For the motion profile, there were increases in the MCS, MRS, ADD as well as the beating rate, all depending on isoproterenol concentrations (Fig. 8C and D). These results suggest that the inotropic, lusitropic and chronotropic effects of isoproterenol can be detected with the motion of hiPS-CM monolayer.

3.4. Variability in contractile data

To test the possibility that contractile parameters of hiPS-CMs detected with the motion vector analysis is critically influenced by the heterogeneity in monolayer preparation, we evaluated the regional variability in MCS and MRS. MCS and MRS were obtained from motion data, and are summarized in Supplementary Fig. 3A and B. The average values of MCS and MRS under control conditions varied from 8 to 15 μm/s and from 4 to 10 μm/s, respectively, and were dependent on the regions of monolayer. These values were altered by the addition of a Ca^{2+} channel blocker, verapamil, which had a negative inotropic effect and similar variability to that of the control. By expressing these values to a percent of the control, we found that each value converged to a similar percentage value (Supplementary Fig. 3A and B). This indicates that the relative values of contractile parameters are significantly less dependent on the region in the preparation.

4. Discussion

The present study aimed to evaluate contractile characteristics and the correlation between contractile motion and electrical properties of hiPS-CM monolayer by using video microscopy, Ca^{2+} transient imaging, traction force microscopy and FP measurement. High resolution motion vector analysis could detect contractile characteristics of hiPS-CMs, i.e., MCS, MRS, ADD and CRD, quantitatively, and demonstrated the correspondence between contractile motion and FP. Motion data further provided complementary information against FP, by detecting the inotropic and lusitropic effects of an experimental drug, isoproterenol. The accessibility to information about relaxation process, or lusitropism, is considered to be one of the advantages of this imaging approach. Recently, there has been increasing attention to the diastolic dysfunction characterized by decreased relaxation velocity and prolonged relaxation and its applicability to common cardiac pathologies, such as ischemic heart diseases and hypertensive heart diseases, and to rare genetic heart diseases, such as DCM [63,64]. The imaging approach could potentially be used to target and analyze hiPS-CMs derived from such diseases.

4.1. Contractile characteristics of hiPS-CMs detected with video microscopy

It has been previously reported that alterations in hiPS-CM area depend on substrate stiffness [26] or cell density [65]. We examined the cell area and the contractile parameters (MCS and MRS) of hiPS-CMs ($n = 40$) and observed no significant dependence of MCS and MRS on cell area. Since in our current study, we sparsely plated hiPS-CMs in order to extract single cell information, average cell area became relatively larger (4244 ± 279 μm^2, $n = 40$) than that recently reported (1654 μm^2, $n = 22$) for hiPS-CMs (iCell CMs) that were plated in a monolayer form with a density of 22,500 cells in the well of a 96-well multiplate [65]. As seen in Fig. 1, the hiPS-CMs attached to the substrate exhibited a heterogeneous shape and their contractile motion often

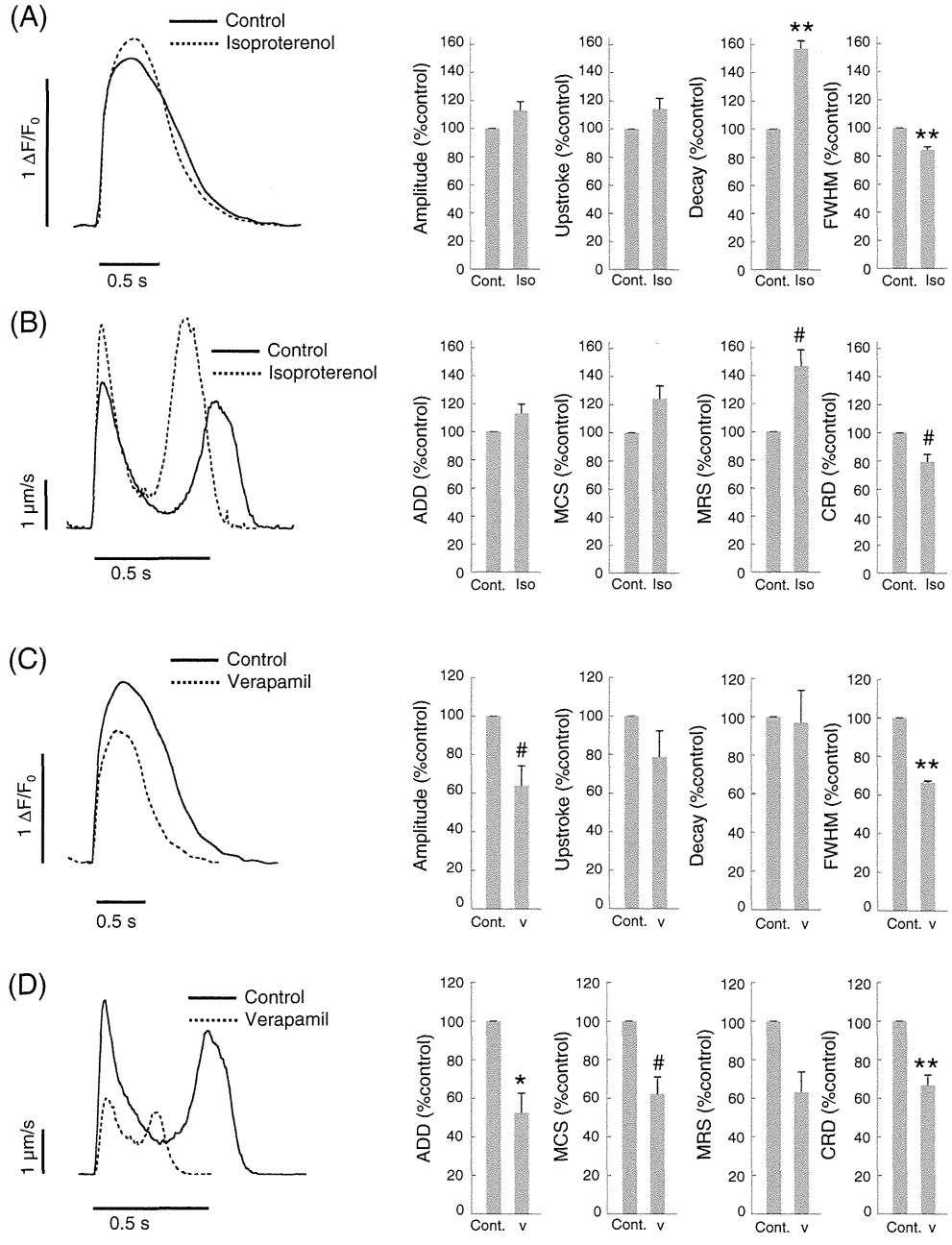

Fig. 3. (A) and (B) show the example profiles of the Ca^{2+} transient and motion waveform of hiPS-CMs, respectively, in the presence of 100 nM isoproterenol. (C) and (D) also show the example profiles of the Ca^{2+} transient and motion waveform of hiPS-CMs, respectively, in the presence of 100 nM verapamil. The bar charts in (A) and (C) represent the drug-induced change in amplitude, maximum upstroke, maximum decay and FWHM of the Ca^{2+}-transient. In (B) and (D), change rate of the contractile parameters, ADD, MCS, MRS and CRD, were also shown in bar charts. The Ca^{2+} transient and motion data were obtained independently. In all the bar charts, values are means ± SE and are expressed as percentage of control.

occurred locally in the cell body. Therefore, it should not be surprising that the average velocity of hiPS-CMs would not correlate well with their cell area. It has been reported that hiPS-CMs cultured for prolonged period, e.g., 90 days, exhibited rod-shaped morphology [66] like adult CMs filled with an aligned sarcomere structure [67]. Those morphologically matured hiPS-CMs, which were not tested in this study, could represent area dependence of contractile speed.

The image-based edge-detection technique has been the method of choice for measuring the shortening of the length of the whole cell body or sarcomere of the rod-shaped adult CMs in order to estimate the force development [34,41–43]. In contrast, TFM has been utilized to assess the contractility of cultured CMs that exhibit an amorphous shape [26,68,69]. With TFM, the traction force of the cells can be estimated based on the deformation of the substrate, which is detected by the displacement of fluorescent beads embedded in the substrate, and on the elastic modulus of the substrate [70]. In our study, we examined the correlation between the force development and cellular deformation (ADD) of the hiPS-CMs. As shown in Fig. 2B, ADD appeared to be correlated with the force development on the substrates (12 kPa and 50 kPa). Phase-contrast microscopy observes

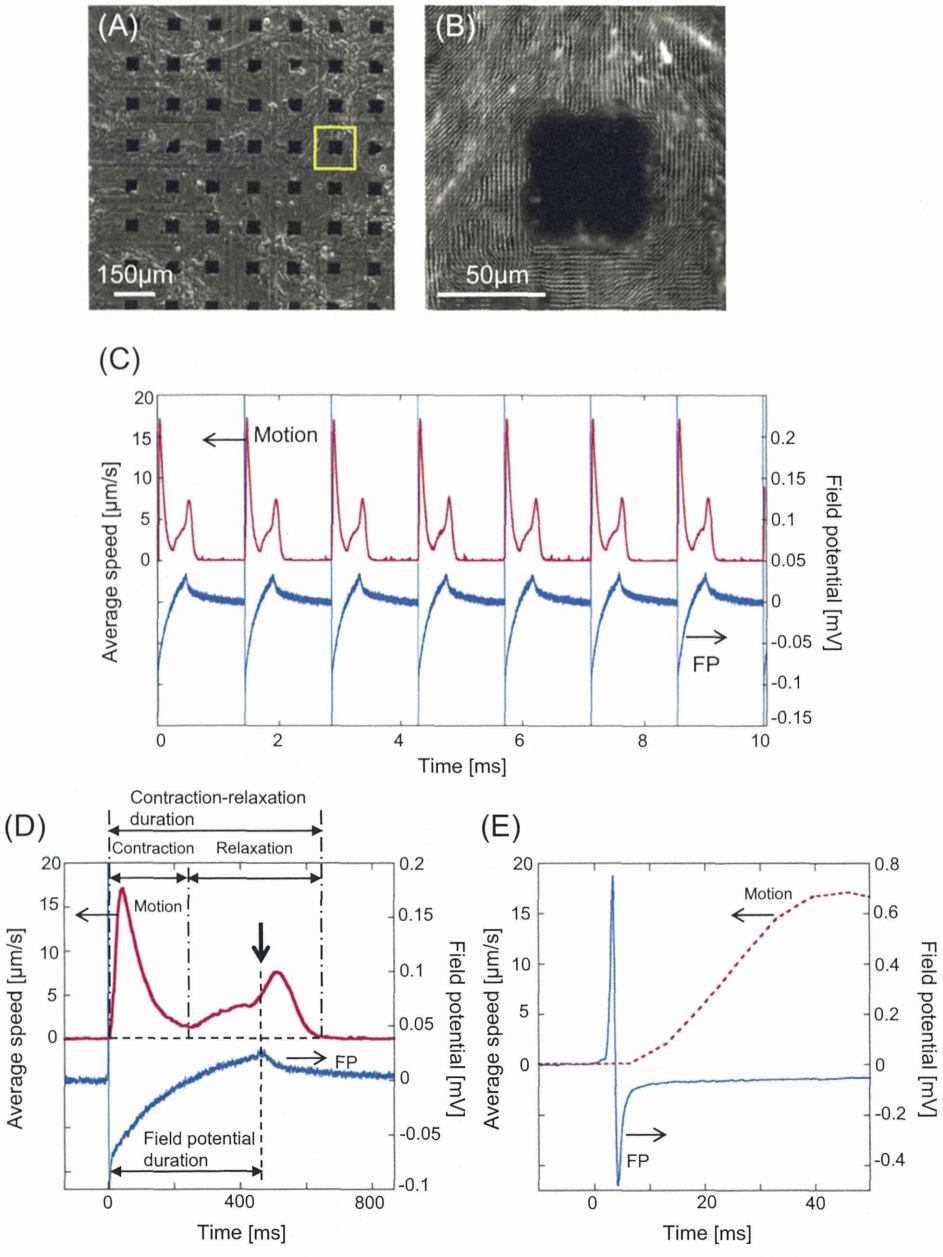

Fig. 4. (A) Phase-contrast image of the hiPS-CM monolayer prepared on the MEA probe. (B) The enlarged velocity field image for the yellow-square region is shown in (A), which shows the motion vectors as fine white lines. (C) Example profile of simultaneously measured hiPS-CM motion and FP. The motion data were evaluated from the region in close vicinity to the electrode (e.g., the yellow-square region in Fig. 4A) that was used for the FP data acquisition. (D) An enlarged single beat profile. The horizontal dashed line represents the baseline of the average velocity (0 μm/s). The vertical dot–dashed lines illustrate the durations of contraction and relaxation of the motion profile. The vertical dashed line with the arrow shows the peak position of positive deflection of the FP. (E) Magnified figure of the onset region of the FP and the motion shown in (D). Time zero corresponds to the onset of the positive FP spike.

overall deformation/displacement of hiPS-CMs during the contraction–relaxation process, including passively moving cellular boundaries and intracellular compartments or organelle. Our present results suggested that the average cellular deformation, ADD, detected by phase-contrast microscopy and motion vector analysis represents the extent of the force development of the hiPS-CMs on the substrates. As long as intra- and extra-cellular elastic properties (e.g., adhesion between hiPS-CMs and substrate) of hiPS-CMs are not altered during the measurement, ADD can be a surrogate marker for the force development of hiPS-CMs.

Isoproterenol and verapamil have been shown to alter the amplitude of the fluorescence peak of the Ca^{2+} transient in iPS-CMs [19]. In our current study, we examined whether the Ca^{2+} transient of hiPS-CMs was correlated with motion behavior in the presence of isoproterenol and verapamil. Responses of the Ca^{2+} transient in hiPS-CMs observed against isoproterenol included an increase in the amplitude, upstroke and decay (Fig. 3A). Interestingly, the maximum decay of the Ca^{2+} transient in the presence of isoproterenol showed a higher increased rate (~160% increase from control) compared to that of maximum upstroke, which is consistent with greater increases in MRS than in MCS of motion

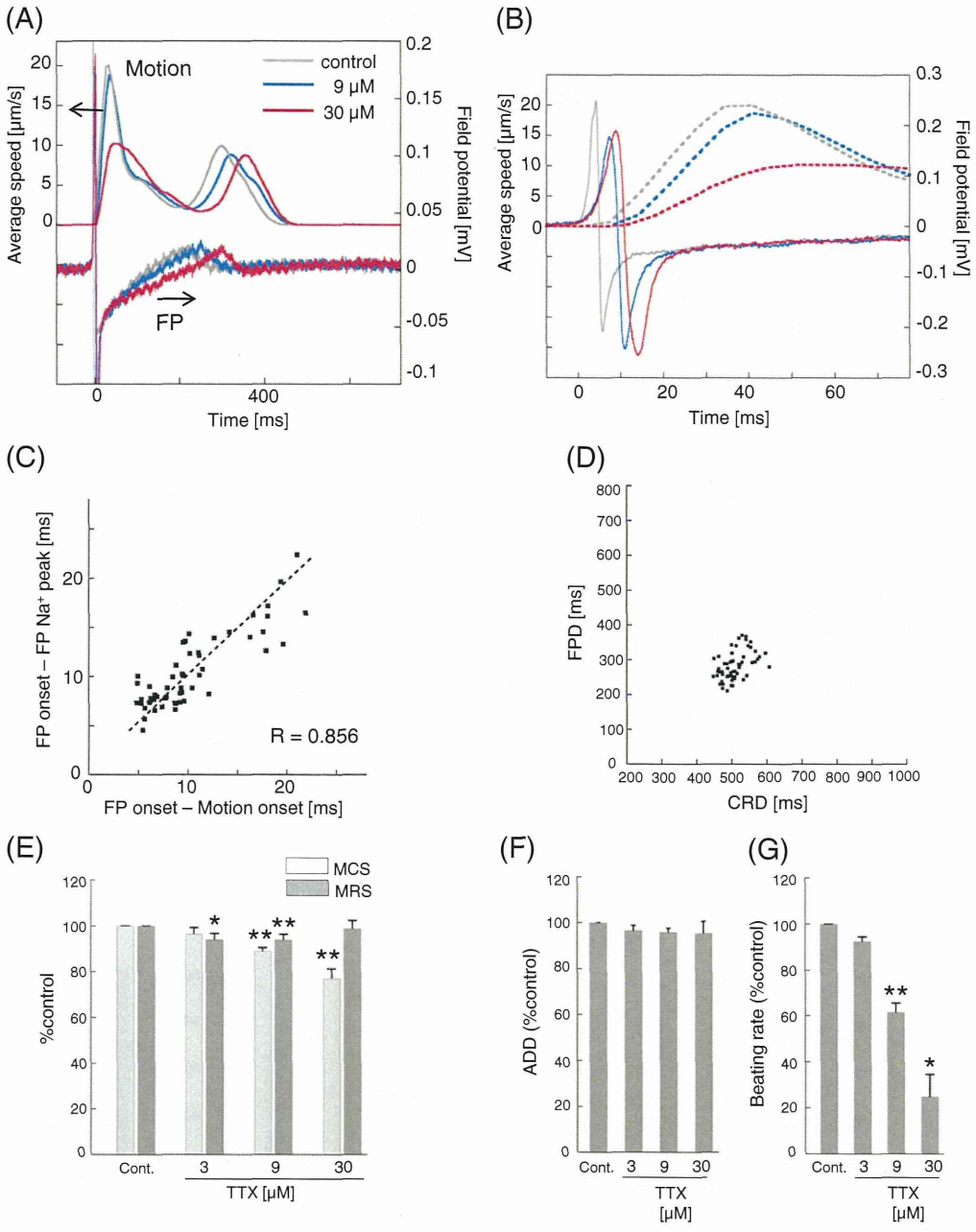

Fig. 5. Contractile and FP responses of the hiPS-CM to tetrodotoxin (TTX). (A) Example of motion and FP profiles of the hiPS-CMs simultaneously measured in the presence of 0, 9, and 30 μM of TTX. (B) Correlation between the CRD and FPD obtained with varied concentrations of TTX (0–30 μM). (C) Enlargement of the onset region of the FP and motion profiles. (D) Correlation of the FP onset-to-FP Na + peak and FP onset-to-motion onset with varied concentrations of TTX (0–30 μM). (E) The normalized change of the MCS and MRS with 0–30 μM of TTX. (F) and (G) show the normalized change of the ADD and beating rate in accordance with the 0–30 μM TTX concentration, respectively. Data were obtained from 15 electrodes with 3 independent preparations and are expressed as means ± SE. $*p < 0.05$; $**p < 0.01$ and $*p < 0.10$ compared with the control.

response. Verapamil decreased all of the parameters of the Ca^{2+} transient in hiPS-CMs (Fig. 3C, D). This is attributed to verapamil's blockage of the L-type Ca^{2+} channel, which is supported by the FP data shown in Fig. 7C. Thus, decreased contraction and relaxation speeds as well as ADD of hiPS-CMs in the presence of verapamil (Fig. 7D and E) can also be attributed to decreased cytoplasmic Ca^{2+} concentration associated with the Ca^{2+}-induced Ca^{2+} release mechanism. Taken together, these data suggest that the cellular deformation in the hiPS-CM monolayer shows a correspondence to the cytoplasmic Ca^{2+} status, observed with a common fluorescence indicator.

4.2. Correlation between the FP and contractile motion of the hiPS-CMs

Our simultaneous measurements of motion and FP confirmed the following correlations under non-arrhythmic conditions: 1) CRD is longer than the FPD; 2) the onset of contraction motion follows the

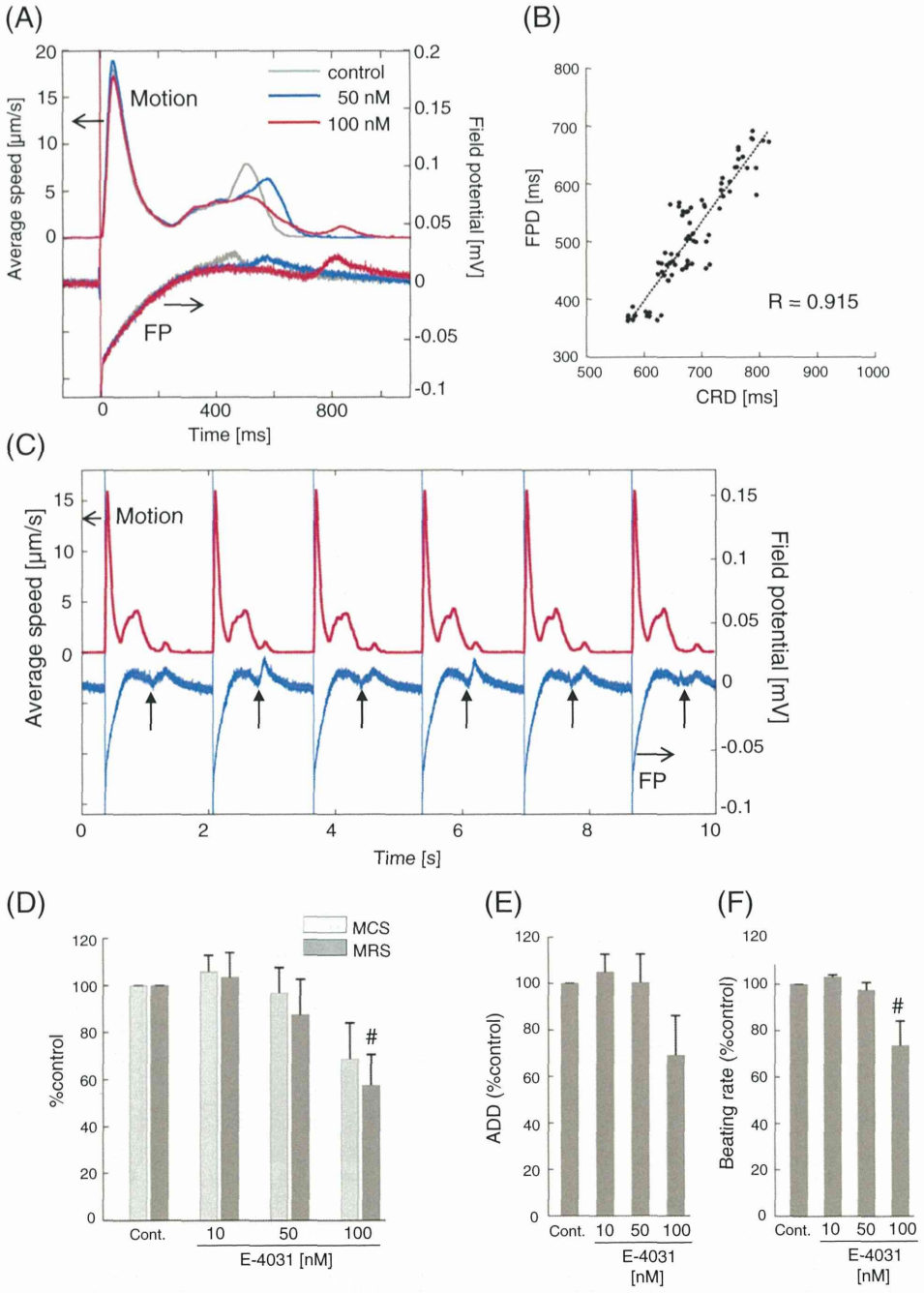

Fig. 6. Contractile and FP responses of the hiPS-CM to E-4031. (A) Example of the motion and FP profiles of the hiPS-CMs simultaneously measured in the presence of 0, 50, and 100 nM of E-4031. (B) Correlation of the CRD and FPD obtained when using varied concentrations of E-4031 (0–~50 nM). Dotted line is a linear regression fitted to the data with R = 0.915 and the slope = 1.362 (FPD/CRD). (C) Relationship between the motion and FP in the presence of 100 nM E-4031. Arrows in (C) indicate the points of the negative deflection in the FP waveform during the relaxation process. Pauses in the relaxation motion corresponded to the negative FP deflections (see also Supplementary Movie 2). (D) Normalized change of the MCS and MRS with 0–100 nM of E-4031. (E) and (F) show the normalized change of the ADD and beating rate in accordance with the 0–100 nM E-4031 concentration changes. Data were obtained from 7 independent preparations of the hiPS-CM monolayer. In (D)–(F), values are expressed as means ± SE. $^{*}p < 0.05$; $^{**}p < 0.01$ and $^{\#}p < 0.10$ compared with the control.

occurrence of the Na^+ current peak of FP; and 3) the position of the negative broad deflection in FP occurs with the contraction. We also observed relationships 1) and 2), but not 3), in neonatal rat CMs. It is noteworthy that while we found the motion profile of hiPS-CMs exhibited a certain amount of displacement (velocity) at the minimum point between contraction and relaxation peak (Figs. 1 and 4), neonatal rat CMs showed almost no displacement (velocity) at the same position (Supplementary Fig. 2). While this observation for the hiPS-CMs appeared to be derived from the lack of any synchronized motion at the end of the contraction, the precise mechanism for this phenomenon remains unclear. Differences in the contraction motion between hiPS-CMs and rat CMs may reflect the presence and absence of the plateau phase

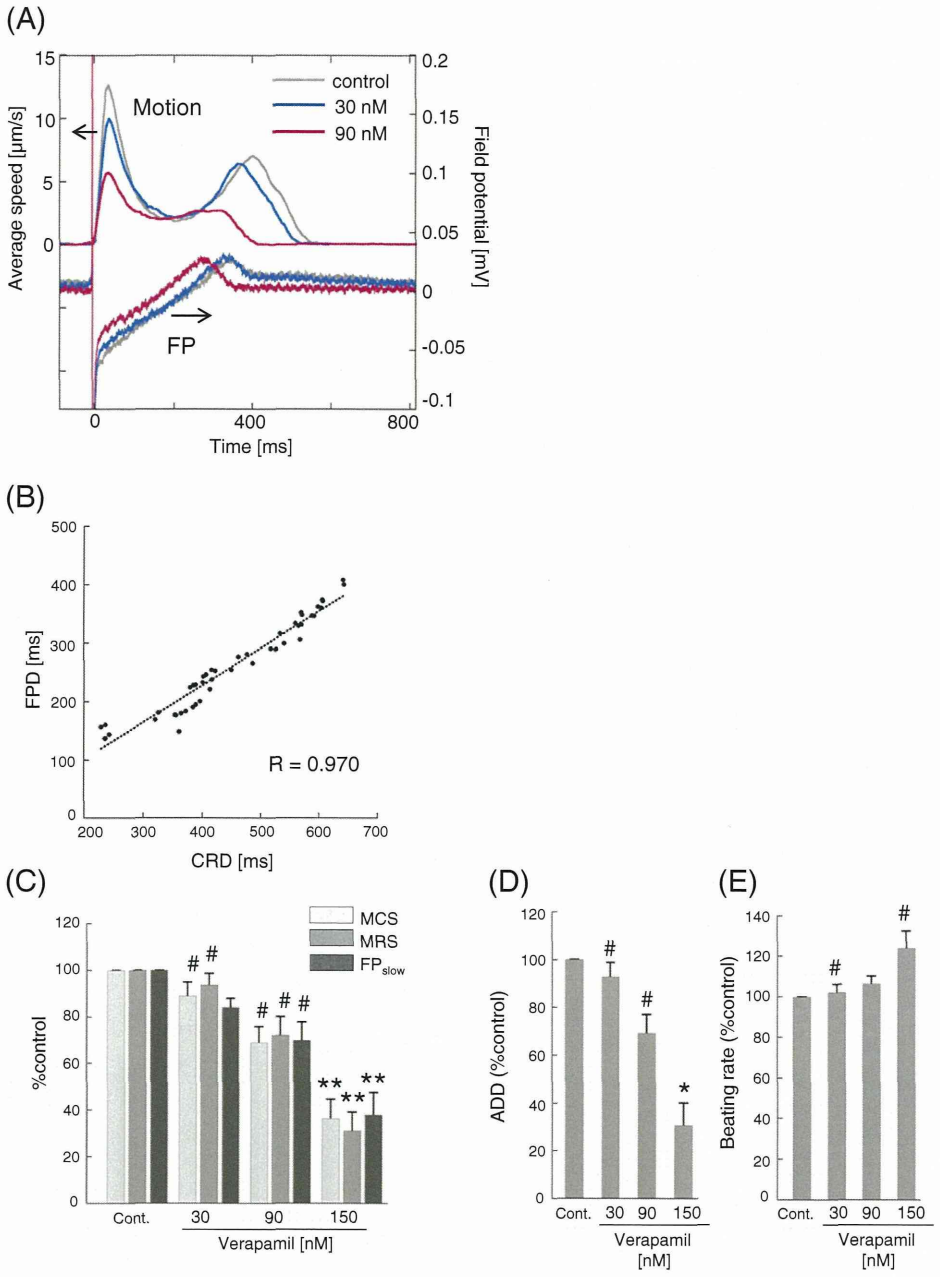

Fig. 7. Contractile and FP responses of the hiPS-CM to verapamil. (A) Example of the motion and FP profiles of the hiPS-CMs simultaneously measured in the presence of 0, 90, and 150 nM of verapamil. (B) Correlation of the CRD and FPD obtained with varied concentrations of verapamil (0–270 nM). Dotted line is a linear regression fitted to the data with R = 0.970 and the slope = 0.633 (FPD/CRD). (C) Change of the rate of the MCS, MRS and the amplitude of FP_{slow}. The amplitude of FP_{slow} was evaluated by averaging the FP value for 6 ms (between 3 ms before and 3 ms after the point of the peak of the contraction motion). (E) and (F) show the normalized change of ADD and beating rate, respectively. Data were obtained from 5 to 8 independent preparations of the hiPS-CM monolayer. In (C)–(E), values are expressed as means ± SE. $^{*}p < 0.05$; $^{**}p < 0.01$ and $^{\#}p < 0.10$ compared with the control.

of their action potential [71–73]. Alternatively, it may be relevant to the immaturity of hiPS-CM sarcoplasmic reticulum, as suggested for hES-CMs [28,29].

We performed a simultaneous measurement of motion and FP from the hiPS-CM monolayer in the presence of TTX, E-4031, verapamil and isoproterenol. The experiments revealed a linear relationship between the CRD and FPD in the presence of E-4031 (10–50 nM), verapamil (30–150 nM) and isoproterenol (0.1–10 μM). Although the slope of the CRD–FPD relationship was suggested to be different in each drug, the present results suggested that the CRD can be a surrogate of the FPD in non-arrhythmic conditions. However, it should be noted that the lower time resolution of motion vector (~6 ms data interval) compared to that of FP (0.05 ms data interval) could be of concern.

Due to the blockage of I_{Kr} with E-4031, it is reasonable to assume that the relaxation speed was decreased at the point where the K^+ current occurred. With regard to the duration, even in the presence of 10–50 nM E-4031, the profile of CRD–FPD correlation appeared to be well correlated with the correlation coefficient of R = 0.915, and the slope of the linear regression was 1.362 (FPD/CRD) (Fig. 6B). This slope value appeared to be significantly larger than the case of verapamil (0.633 (FPD/CRD)) shown in Fig. 7B. This may be relevant to the abnormalities in electro-mechanical relationship reported for the Torsade

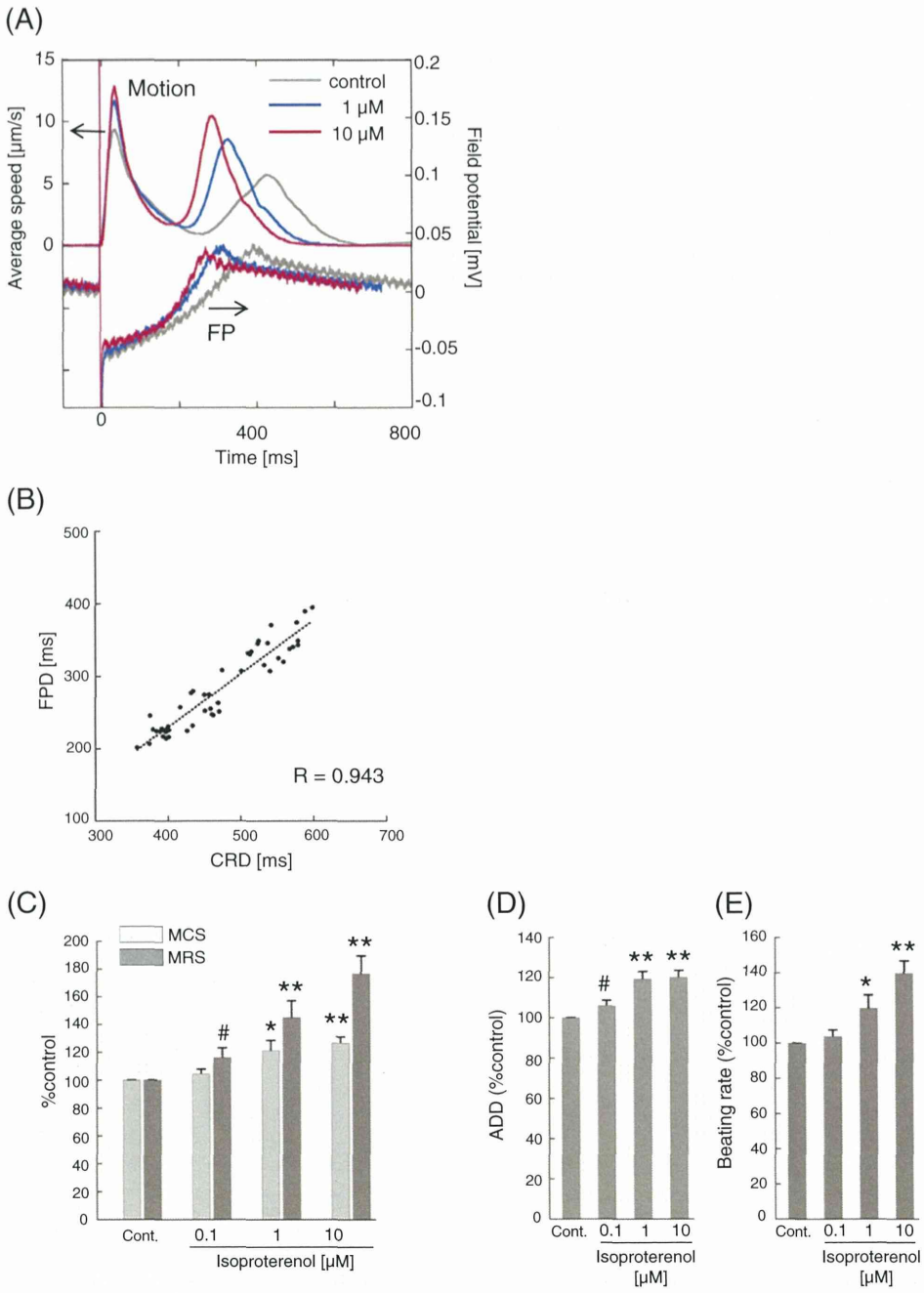

Fig. 8. Contractile and FP responses of the hiPS-CM to isoproterenol. (A) Example of the motion and FP profiles of the hiPS-CMs simultaneously measured in the presence of 0, 1, and 10 μM of isoproterenol. (B) Correlation of the CRD and FPD obtained when using various concentrations of isoproterenol (0–10 μM). Dotted line is a linear regression fitted to the data with R = 0.943 and the slope = 0.738 (FPD/CRD). (C) Normalized change of the MCS and MRS with 0–10 μM of isoproterenol. (D) and (E) show the normalized change of the ADD and beating rate, respectively. Data were evaluated from 7 independent preparations of the hiPS-CM monolayer. In (C)–(E), values are expressed as means ± SE. $^{*}p < 0.05$; $^{**}p < 0.01$ and $^{\#}p < 0.10$ compared with the control.

de Pointes-genic drugs [74–76]. However, to determine the precise relation between FPD and CRD, it is necessary to determine FPD accurately even when the extensive broadening occurred and to consider the beating rate, which is beyond the scope of the present paper and is needed to be examined in a further study. In the presence of 50–100 nM E-4031, the EAD-like negative deflection in the FP waveform was observed. EADs are caused by the re-activation of the inactivated L-type Ca^{2+} current or the inactivated voltage-dependent Na^{+} current, with the latter associated with the activation of the forward cycle of the Na^{+}/Ca^{2+} exchanger and the resultant Ca^{2+} influx. Thus, it is conceivable that the EAD is associated with the transient increase in the intracellular Ca^{2+} concentration, which leads to a reduction of the relaxation motion speed before completion of the relaxation process, thereby resulting in the appearance of another motion peak at the end of relaxation (Fig. 6C). As recognized in the video images of hiPS-CMs in the presence of 100 nM E-4031 (Supplementary video 2), however, such additional single peaks were a part of relaxation motion, not of an independent contraction–relaxation motion. After the occurrence of this type of two-step relaxation motion, triggered activity followed by arrhythmic beating were often observed (data not

shown). EAD-induced contraction, or triggered activity, was also reported using a video edge-detection system for hiPS-CMs in the presence of E-4031 [77]. The occurrence of another motion peak at the end of relaxation could be a potential marker for the early detection of EAD.

Verapamil increased the beating rate of hiPS-CM (Fig. 7E). Although this effect would not be expected to occur based on verapamil's mechanism of action and previous clinical findings [78–80], verapamil has been reported to have a positive chronotropic effect on hES-CMs [54]. In accordance with the concentration of verapamil used in the current study, decreases were observed in MCS and in the amplitude of FP_{slow}. FP_{slow} was also decreased under Ca^{2+}-free condition in embryonic mouse CMs and was suggested to reflect the current of L-type Ca^{2+} channel [55]. Although FP_{slow} does not solely represent the extent of the Ca^{2+} current, their relative values (% of control) were in good agreement with those of the MCS.

Isoproterenol was also observed to increase beating rate, MCS, MRS and ADD. The increasing rate of maximum velocity was greater during relaxation (176% at 10 μM, $n = 7$) versus that during contraction (126% at 10 μM, $n = 7$) (Fig. 8C). Although the precise reason for these findings is currently unknown, Turnbull et al. described the negligible inotropic response of hES-CMs against isoproterenol and pointed out the immaturity of the sarcoplasmic reticulum of the hES-CMs [29]. Pillekampt et al. also reported that isoproterenol significantly induced positive chronotropy and lusitropy but not inotropy in early hES-CMs [28]. The mechanism underlying the hES-CMs findings in their study could be relevant to our current hiPS-CM observations. On the other hand, the FP profile showed no major alterations by the addition of isoproterenol with the exception of the shortening in FPD. Although the L-type Ca^{2+} channel is one of the targets of the isoproterenol action, alterations in FP_{slow} were not clearly detected with isoproterenol. This could be partly due to that negative deflection in FP does not solely reflect the L-type Ca^{2+} current, since the FP is an extracellular potential and not a cell membrane potential.

4.3. Variability in the contractile data

To some extent, the absolute values of MCS and MRS of hiPS-CMs depend on the monolayer region (Supplementary Fig. 3A). The reasons for this regional heterogeneity can be considered to be as follows: 1) the cell density may not be thoroughly homogeneous in the well, 2) the cell size and contractile characteristics have some variability, 3) the hiPS-CM monolayer contains a certain amount of non-cardiac (non-contracting) cells (~2%), and 4) the monolayer preparations contain a variety of shapes and types (atrial-, ventricular- and nodal-type) of hiPS-CMs. However, as long as we evaluate the contractile parameters from the same field of view in the monolayer and express the parameters using a relative value (i.e., % of the control), the inter-region variability of the contractile parameters should be fairly small (Supplementary Fig. 3B). It is possible that non-cardiac cells may have affected the contractile properties of our cultures because those cells move passively with lower motion speed than that of contracting hiPS-CMs. However, we assumed that they were present to a similar extent in all regions in the monolayer and hence should not have affected the validity of our results.

In conclusion, this study demonstrated that the contractile motion of 2D cultured hiPS-CMs, detected by a high-speed camera and motion vector analysis, quantitatively corresponded to their electrophysiological and functional behaviors under non-arrhythmic condition. Although the relationship between hiPS-CM motion and FP during excitation–contraction decoupling or proarrhythmic conditions is of great interest, it is not within the scope of this current paper and will need to be examined in a further study. The results of the present study will open up the possibilities of detecting cellular-level information on the electric and mechanical relationship of cultured CMs and will contribute to expand the applicability of hiPS-CMs in the field of cellular cardiology, drug screening and cardiac therapeutics.

Supplementary data to this article can be found online at http://dx.doi.org/10.1016/j.yjmcc.2014.09.010.

Disclosure Statement

T.H., T.K., S.K., E.M. and H.Y. are employed by Sony Corporation.

References

[1] Habib M, Caspi O, Gepstein L. Human embryonic stem cells for cardiomyogenesis. J Mol Cell Cardiol Oct 2008;45(4):462–74.
[2] Caspi O, Itzhaki I, Kehat I, Gepstein A, Arbel G, Huber I, et al. In vitro electrophysiological drug testing using human embryonic stem cell derived cardiomyocytes. Stem Cells Dev Jan–Feb 2009;18(1):161–72.
[3] Tanaka T, Tohyama S, Murata M, Nomura F, Kaneko T, Chen H, et al. In vitro pharmacologic testing using human induced pluripotent stem cell-derived cardiomyocytes. Biochem Biophys Res Commun Aug 7 2009;385(4):497–502.
[4] Guo L, Abrams RM, Babiarz JE, Cohen JD, Kameoka S, Sanders MJ, et al. Estimating the risk of drug-induced proarrhythmia using human induced pluripotent stem cell-derived cardiomyocytes. Toxicol Sci Sep 2011;123(1):281–9.
[5] Kadota S, Minami I, Morone N, Heuser JE, Agladze K, Nakatsuji N. Development of a reentrant arrhythmia model in human pluripotent stem cell-derived cardiac cell sheets. Eur Heart J Apr 2013;34(15):1147–56.
[6] Nakamura Y, Matsuo J, Miyamoto N, Ojima A, Ando K, Kanda Y, et al. Assessment of testing methods for drug-induced repolarization delay and arrhythmias in an iPS cell-derived cardiomyocyte sheet: multi-site validation study. J Pharmacol Sci 2014;124(4):494–501.
[7] Caspi O, Lesman A, Basevitch Y, Gepstein A, Arbel G, Habib IH, et al. Tissue engineering of vascularized cardiac muscle from human embryonic stem cells. Circ Res Feb 2 2007;100(2):263–72.
[8] Yoshida Y, Yamanaka S. iPS cells: a source of cardiac regeneration. J Mol Cell Cardiol Feb 2011;50(2):327–32.
[9] Kawamura M, Miyagawa S, Fukushima S, Saito A, Miki K, Ito E, et al. Enhanced survival of transplanted human induced pluripotent stem cell-derived cardiomyocytes by the combination of cell sheets with the pedicled omental flap technique in a porcine heart. Circulation Sep 10 2013;128(11 Suppl. 1):S87–94.
[10] Sawa Y, Miyagawa S. Present and future perspectives on cell sheet-based myocardial regeneration therapy. BioMed Res Int 2013;2013:583912.
[11] Matsuura K, Haraguchi Y, Shimizu T, Okano T. Cell sheet transplantation for heart tissue repair. J Control Release Aug 10 2013;169(3):336–40.
[12] Itzhaki I, Schiller J, Beyar R, Satin J, Gepstein L. Calcium handling in embryonic stem cell-derived cardiac myocytes: of mice and men. Ann N Y Acad Sci Oct 2006;1080:207–15.
[13] Satin J, Itzhaki I, Rapoport S, Schroder EA, Izu L, Arbel G, et al. Calcium handling in human embryonic stem cell-derived cardiomyocytes. Stem Cells Aug 2008;26(8):1961–72.
[14] Zwi L, Caspi O, Arbel G, Huber I, Gepstein A, Park IH, et al. Cardiomyocyte differentiation of human induced pluripotent stem cells. Circulation Oct 13 2009;120(15):1513–23.
[15] Itzhaki I, Rapoport S, Huber I, Mizrahi I, Zwi-Dantsis L, Arbel G, et al. Calcium handling in human induced pluripotent stem cell derived cardiomyocytes. PLoS One 2011;6(4):e18037.
[16] Lee YK, Ng KM, Lai WH, Chan YC, Lau YM, Lian Q, et al. Calcium homeostasis in human induced pluripotent stem cell-derived cardiomyocytes. Stem Cell Rev Nov 2011;7(4):976–86.
[17] Jonsson MK, Vos MA, Mirams GR, Duker G, Sartipy P, de Boer TP, et al. Application of human stem cell-derived cardiomyocytes in safety pharmacology requires caution beyond hERG. J Mol Cell Cardiol May 2012;52(5):998–1008.
[18] Zhang GQ, Wei H, Lu J, Wong P, Shim W. Identification and characterization of calcium sparks in cardiomyocytes derived from human induced pluripotent stem cells. PLoS One 2013;8(2):e55266.
[19] Sirenko O, Crittenden C, Callamaras N, Hesley J, Chen YW, Funes C, et al. Multiparameter in vitro assessment of compound effects on cardiomyocyte physiology using iPSC cells. J Biomol Screen Jan 2013;18(1):39–53.
[20] Navarrete EG, Liang P, Lan F, Sanchez-Freire V, Simmons C, Gong T, et al. Screening drug-induced arrhythmia events using human induced pluripotent stem cell-derived cardiomyocytes and low-impedance microelectrode arrays. Circulation Sep 10 2013;128(11 Suppl. 1):S3–S13.
[21] Xi J, Khalil M, Shishechian N, Hannes T, Pfannkuche K, Liang H, et al. Comparison of contractile behavior of native murine ventricular tissue and cardiomyocytes derived from embryonic or induced pluripotent stem cells. FASEB J Aug 2010;24(8):2739–51.
[22] Hansen A, Eder A, Bonstrup M, Flato M, Mewe M, Schaaf S, et al. Development of a drug screening platform based on engineered heart tissue. Circ Res Jul 9 2010;107(1):35–44.
[23] Liau B, Christoforou N, Leong KW, Bursac N. Pluripotent stem cell-derived cardiac tissue patch with advanced structure and function. Biomaterials Dec 2011;32(35):9180–7.
[24] Schaaf S, Shibamiya A, Mewe M, Eder A, Stohr A, Hirt MN, et al. Human engineered heart tissue as a versatile tool in basic research and preclinical toxicology. PLoS One 2011;6(10):e26397.

[25] Tulloch NL, Muskheli V, Razumova MV, Korte FS, Regnier M, Hauch KD, et al. Growth of engineered human myocardium with mechanical loading and vascular coculture. Circ Res Jun 24 2011;109(1):47–59.
[26] Hazeltine LB, Simmons CS, Salick MR, Lian X, Badur MG, Han W, et al. Effects of substrate mechanics on contractility of cardiomyocytes generated from human pluripotent stem cells. Int J Cell Biol 2012;2012:508294.
[27] Liu J, Sun N, Bruce MA, Wu JC, Butte MJ. Atomic force mechanobiology of pluripotent stem cell-derived cardiomyocytes. PLoS One 2012;7(5):e37559.
[28] Pillekamp F, Haustein M, Khalil M, Emmelheinz M, Nazzal R, Adelmann R, et al. Contractile properties of early human embryonic stem cell-derived cardiomyocytes: beta-adrenergic stimulation induces positive chronotropy and lusitropy but not inotropy. Stem Cells Dev Aug 10 2012;21(12):2111–21.
[29] Turnbull IC, Karakikes I, Serrao GW, Backeris P, Lee JJ, Xie C, et al. Advancing functional engineered cardiac tissues toward a preclinical model of human myocardium. FASEB J Feb 2014;28(2):644–54.
[30] Sun N, Yazawa M, Liu J, Han L, Sanchez-Freire V, Abilez OJ, et al. Patient-specific induced pluripotent stem cells as a model for familial dilated cardiomyopathy. Sci Transl Med Apr 18 2012;4(130):130ra47.
[31] Tameyasu T, Toyoki T, Sugi H. Nonsteady motion in unloaded contractions of single frog cardiac cells. Biophys J Sep 1985;48(3):461–5.
[32] O'Rourke B, Reibel DK, Thomas AP. High-speed digital imaging of cytosolic Ca^{2+} and contraction in single cardiomyocytes. Am J Physiol Jul 1990;259(1 Pt 2):H230–42.
[33] Pollack PS, Carson NL, Nuss HB, Marino TA, Houser SR. Mechanical properties of adult feline ventricular myocytes in culture. Am J Physiol Jan 1991;260(1 Pt 2): H234–41.
[34] Mukherjee R, Crawford FA, Hewett KW, Spinale FG. Cell and sarcomere contractile performance from the same cardiocyte using video microscopy. J Appl Physiol Apr 1993;74(4):2023–33.
[35] Stummann TC, Wronski M, Sobanski T, Kumpfmueller B, Hareng L, Bremer S, et al. Digital movie analysis for quantification of beating frequencies, chronotropic effects, and beating areas in cardiomyocyte cultures. Assay Drug Dev Technol Jun 2008; 6(3):375–85.
[36] Kamgoue A, Ohayon J, Usson Y, Riou L, Tracqui P. Quantification of cardiomyocyte contraction based on image correlation analysis. Cytometry A Apr 2009;75(4): 298–308.
[37] Bazan C, Barba DT, Blomgren P, Paolini P. Image processing techniques for assessing contractility in isolated adult cardiac myocytes. Int J Biomed imaging 2009;2009: 352954.
[38] Bazan C, Torres Barba D, Blomgren P, Paolini P. Image processing techniques for assessing contractility in isolated neonatal cardiac myocytes. Int J Biomed imaging 2011;2011:729732.
[39] Hossain MM, Shimizu E, Saito M, Rao SR, Yamaguchi Y, Tamiya E. Non-invasive characterization of mouse embryonic stem cell derived cardiomyocytes based on the intensity variation in digital beating video. Analyst Jul 2010;135(7):1624–30.
[40] Harmer AR, Abi-Gerges N, Morton MJ, Pullen GF, Valentin JP, Pollard CE. Validation of an in vitro contractility assay using canine ventricular myocytes. Toxicol Appl Pharmacol Apr 15 2012;260(2):162–72.
[41] Harding SE, Vescovo G, Kirby M, Jones SM, Gurden J, Poole-Wilson PA. Contractile responses of isolated adult rat and rabbit cardiac myocytes to isoproterenol and calcium. J Mol Cell Cardiol Jul 1988;20(7):635–47.
[42] Vescovo G, Harding SE, Jones SM, Dalla Libera L, Pessina AC, Poole-Wilson PA. Comparison between isomyosin pattern and contractility of right ventricular myocytes isolated from rats with right cardiac hypertrophy. Basic Res Cardiol Sep–Oct 1989; 84(5):536–43.
[43] Steadman BW, Moore KB, Spitzer KW, Bridge JH. A video system for measuring motion in contracting heart cells. IEEE Trans Biomed Eng Apr 1988;35(4):264–72.
[44] He JQ, Ma Y, Lee Y, Thomson JA, Kamp TJ. Human embryonic stem cells develop into multiple types of cardiac myocytes: action potential characterization. Circ Res Jul 11 2003;93(1):32–9.
[45] Brito-Martins M, Harding SE. Ali NN. beta(1)- and beta(2)-adrenoceptor responses in cardiomyocytes derived from human embryonic stem cells: comparison with failing and non-failing adult human heart. Br J Pharmacol Feb 2008;153(4):751–9.
[46] Ahola A, Kiviaho AL, Larsson K, Honkanen M, Aalto-Setala K, Hyttinen J. Video image-based analysis of single human induced pluripotent stem cell derived cardiomyocyte beating dynamics using digital image correlation. Biomed Eng Online 2014;13(1): 39.
[47] Hayakawa T, Kunihiro T, Dowaki S, Uno H, Matsui E, Uchida M, et al. Noninvasive evaluation of contractile behavior of cardiomyocyte monolayers based on motion vector analysis. Tissue Eng Part C Methods Jan 2012;18(1):21–32.
[48] Ma J, Guo L, Fiene SJ, Anson BD, Thomson JA, Kamp TJ, et al. High purity human-induced pluripotent stem cell-derived cardiomyocytes: electrophysiological properties of action potentials and ionic currents. Am J Physiol Nov 2011;301(5):H2006–17.
[49] Ghanbari M. The cross-search algorithm for motion estimation. Trans Commun 1990;38(7):950–3.
[50] Dembo M, Wang YL. Stresses at the cell-to-substrate interface during locomotion of fibroblasts. Biophys J Apr 1999;76(4):2307–16.
[51] Sabass B, Gardel ML, Waterman CM, Schwarz US. High resolution traction force microscopy based on experimental and computational advances. Biophys J Jan 1 2008;94(1):207–20.
[52] Tseng Q, Duchemin-Pelletier E, Deshiere A, Balland M, Guillou H, Filhol O, et al. Spatial organization of the extracellular matrix regulates cell–cell junction positioning. Proc Natl Acad Sci U S A Jan 31 2012;109(5):1506–11.
[53] Butler JP, Tolic-Norrelykke IM, Fabry B, Fredberg JJ. Traction fields, moments, and strain energy that cells exert on their surroundings. Am J Physiol Cell Physiol Mar 2002;282(3):C595–605.
[54] Yamazaki K, Hihara T, Taniguchi T, Kohmura N, Yoshinaga T, Ito M, et al. A novel method of selecting human embryonic stem cell-derived cardiomyocyte clusters for assessment of potential to influence QT interval. Toxicol In Vitro Mar 2012; 26(2):335–42.
[55] Halbach M, Egert U, Hescheler J, Banach K. Estimation of action potential changes from field potential recordings in multicellular mouse cardiac myocyte cultures. Cell Physiol Biochem 2003;13(5):271–84.
[56] Meyer T, Boven KH, Gunther E, Fejtl M. Micro-electrode arrays in cardiac safety pharmacology: a novel tool to study QT interval prolongation. Drug Saf 2004; 27(11):763–72.
[57] Egert U, Meyer T. Heart on a chip – extracellular multielectrode recordings from cardiomyocytes in vitro; 2005.
[58] Reppel M, Igelmund P, Egert U, Juchelka F, Hescheler J, Drobinskaya I. Effect of cardioactive drugs on action potential generation and propagation in embryonic stem cell-derived cardiomyocytes. Cell Physiol Biochem 2007;19(5–6):213–24.
[59] Liang H, Matzkies M, Schunkert H, Tang M, Bonnemeier H, Hescheler J, et al. Human and murine embryonic stem cell-derived cardiomyocytes serve together as a valuable model for drug safety screening. Cell Physiol Biochem 2010;25(4–5):459–66.
[60] Matsa E, Rajamohan D, Dick E, Young L, Mellor I, Staniforth A, et al. Drug evaluation in cardiomyocytes derived from human induced pluripotent stem cells carrying a long QT syndrome type 2 mutation. Eur Heart J Apr 2011;32(8):952–62.
[61] Braam SR, Tertoolen L, van de Stolpe A, Meyer T, Passier R, Mummery CL. Prediction of drug-induced cardiotoxicity using human embryonic stem cell-derived cardiomyocytes. Stem Cell Res Mar 2009;4(2):107–16.
[62] Nomura F, Kaneko T, Hattori A, Yasuda K. On-chip constructive cell-network study (II): on-chip quasi-in vivo cardiac toxicity assay for ventricular tachycardia/fibrillation measurement using ring-shaped closed circuit microelectrode with lined-up cardiomyocyte cell network. J Nanobiotechnol 2011;9:39.
[63] Periasamy M, Bhupathy P, Babu GJ. Regulation of sarcoplasmic reticulum Ca^{2+} ATPase pump expression and its relevance to cardiac muscle physiology and pathology. Cardiovasc Res Jan 15 2008;77(2):265–73.
[64] Borlaug BA, Kass DA. Mechanisms of diastolic dysfunction in heart failure. Trends Cardiovasc Med Nov 2006;16(8):273–9.
[65] Uesugi M, Ojima A, Taniguchi T, Miyamoto N, Sawada K. Low-density plating is sufficient to induce cardiac hypertrophy and electrical remodeling in highly purified human iPS cell-derived cardiomyocytes. J Pharmacol Toxicol Methods 2014;69(2): 177–88.
[66] Shinozawa T, Imahashi K, Sawada H, Furukawa H, Takami K. Determination of appropriate stage of human-induced pluripotent stem cell-derived cardiomyocytes for drug screening and pharmacological evaluation in vitro. J Biomol Screen Oct 2012;17(9):1192–203.
[67] Bird SD, Doevendans PA, van Rooijen MA, Brutel de la Riviere A, Hassink RJ, Passier R, et al. The human adult cardiomyocyte phenotype. Cardiovasc Res May 1 2003;58(2): 423–34.
[68] Bhana B, Iyer RK, Chen WL, Zhao R, Sider KL, Likhitpanichkul M, et al. Influence of substrate stiffness on the phenotype of heart cells. Biotechnol Bioeng Apr 15 2010; 105(6):1148–60.
[69] Hersch N, Wolters B, Dreissen G, Springer R, Kirchgessner N, Merkel R, et al. The constant beat: cardiomyocytes adapt their forces by equal contraction upon environmental stiffening. Biol Open Mar 15 2013;2(3):351–61.
[70] Wang JH, Lin JS. Cell traction force and measurement methods. Biomech Model Mechanobiol Nov 2007;6(6):361–71.
[71] Langer GA, Brady AJ, Tan ST, Serena D. Correlation of the glycoside response, the force staircase, and the action potential configuration in the neonatal rat heart. Circ Res Jun 1975;36(6):744–52.
[72] Zhang J, Wilson GF, Soerens AG, Koonce CH, Yu J, Palecek SP, et al. Functional cardiomyocytes derived from human induced pluripotent stem cells. Circ Res Feb 27 2009;104(4):e30–41.
[73] Honda M, Kiyokawa J, Tabo M, Inoue T. Electrophysiological characterization of cardiomyocytes derived from human induced pluripotent stem cells. J Pharmacol Sci 2011;117(3):149–59.
[74] van der Linde HJ, Van Deuren B, Somers Y, Loenders B, Towart R, Gallacher DJ. The electro-mechanical window: a risk marker for Torsade de Pointes in a canine model of drug induced arrhythmias. Br J Pharmacol Dec 2010;161(7):1444–54.
[75] Guns PJ, Johnson DM, Van Op den Bosch J, Weltens E, Lissens J. The electro-mechanical window in anaesthetized guinea pigs: a new marker in screening for Torsade de Pointes risk. Br J Pharmacol May 2012;166(2):689–701.
[76] Guns PJ, Johnson DM, Weltens E, Lissens J. Negative electro-mechanical windows are required for drug-induced Torsades de Pointes in the anesthetized guinea pig. J Pharmacol Toxicol Methods Sep 2012;66(2):125–34.
[77] Doss MX, Di Diego JM, Goodrow RJ, Wu Y, Cordeiro JM, Nesterenko VV, et al. Maximum diastolic potential of human induced pluripotent stem cell-derived cardiomyocytes depends critically on I(Kr). PLoS One 2012;7(7):e40288.
[78] Wellens HJ, Tan SL, Bar FW, Duren DR, Lie KI, Dohmen HM. Effect of verapamil studied by programmed electrical stimulation of the heart in patients with paroxysmal re-entrant supraventricular tachycardia. Br Heart J Oct 1977;39(10):1058–66.
[79] Gay R, Algeo S, Lee R, Olajos M, Morkin E, Goldman S. Treatment of verapamil toxicity in intact dogs. J Clin Invest Jun 1986;77(6):1805–11.
[80] Nazzaro P, Manzari M, Merlo M, Triggiani R, Scarano AM, Lasciarrea A, et al. Antihypertensive treatment with verapamil and amlodipine. Their effect on the functional autonomic and cardiovascular stress responses. Eur Heart J Sep 1995;16(9):1277–84.

SCIENTIFIC REPORTS

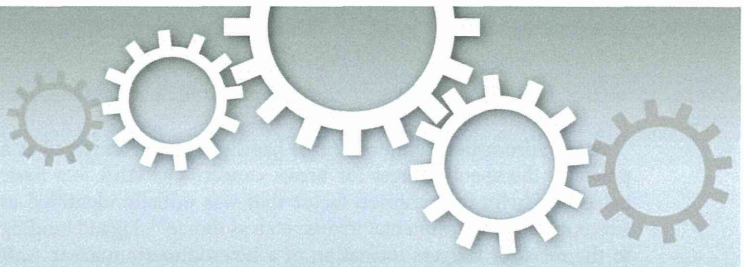

OPEN

SUBJECT AREAS:
CHEMOTHERAPY
BREAST CANCER

Received
16 July 2014

Accepted
29 October 2014

Published
18 November 2014

Correspondence and requests for materials should be addressed to H.H. (hiromi_hiyoshi@tara.tsukuba.ac.jp)

2-(4-Hydroxy-3-methoxyphenyl)-benzothiazole suppresses tumor progression and metastatic potential of breast cancer cells by inducing ubiquitin ligase CHIP

Hiromi Hiyoshi[1,2], Natsuka Goto[1], Mai Tsuchiya[1], Keisuke Iida[3], Yuka Nakajima[1,2], Naoya Hirata[4], Yasunari Kanda[4], Kazuo Nagasawa[3] & Junn Yanagisawa[1,2]

[1]Graduate School of Life and Environmental Sciences, University of Tsukuba, 1-1-1 Tennodai, Tsukuba 305-8577, Japan, [2]Center for Tsukuba Advanced Research Alliance, University of Tsukuba, 1-1-1 Tennodai, Tsukuba 305-8577, Japan, [3]Faculty of Technology, Tokyo University of Agriculture and Technology-TUAT, 2-24-16 Naka-cho, Koganei-shi, Tokyo 185-0031, Japan, [4]Division of Pharmacology, National Institute of Health Sciences, 1-18-1, Kamiyoga, Setagaya-ku 158-8501, Japan.

Breast cancer is the most common malignancy among women and has poor survival and high recurrence rates for aggressive metastatic disease. Notably, triple-negative breast cancer (TNBC) is a highly aggressive cancer and there is no preferred agent for TNBC therapy. In this study, we show that a novel agent, 2-(4-hydroxy-3-methoxyphenyl)-benzothiazole (YL-109), has ability to inhibit breast cancer cell growth and invasiveness *in vitro* and *in vivo*. In addition, YL-109 repressed the sphere-forming ability and the expression of stem cell markers in MDA-MB-231 mammosphere cultures. YL-109 increased the expression of carboxyl terminus of Hsp70-interacting protein (CHIP), which suppresses tumorigenic and metastatic potential of breast cancer cells by inhibiting the oncogenic pathway. YL-109 induced *CHIP* transcription because of the recruitment of the aryl hydrocarbon receptor (AhR) to upstream of *CHIP* gene in MDA-MB-231 cells. Consistently, the antitumor effects of YL-109 were depressed by *CHIP* or *AhR* knockdown in MDA-MB-231 cells. Taken together, our findings indicate that a novel agent YL-109 inhibits cell growth and metastatic potential by inducing CHIP expression through AhR signaling and reduces cancer stem cell properties in MDA-MB-231 cells. It suggests that YL-109 is a potential candidate for breast cancer therapy.

Breast cancer is the major cause of cancer death among women worldwide. Triple-negative breast cancer (TNBC), which has been reported to represent approximately 15% of all breast cancers[1], is characterized by the absence of estrogen receptors (ERs), progesterone receptors (PRs), and human epidermal growth factor-2 (HER-2) expression[2]. TNBC is an aggressive cancer, characterized by rapid tumor growth, a high incidence of metastasis, an increased rate of distant recurrence, and a poor prognosis compared with other breast cancer subtypes[3]. Unlike ER/PR-positive or HER-2-overexpressing subtypes, the effective treatment options for TNBC are limited to cytotoxic therapies because of the lack of molecular targets. Moreover, TNBC cells show a profile that is similar to breast cancer stem cells, which have a strong resistance to chemotherapeutic drugs[4,5]. Therefore, new therapeutic options and strategies are required for TNBC therapy.

The carboxyl terminus of Hsp70-interacting protein (CHIP, also named STUB1) is a potential target for the treatment of TNBC. CHIP is a U-box-type ubiquitin E3 ligase that induces ubiquitylation and degradation of its substrates. These include several oncogenic proteins that suppress the tumorigenic and metastatic potential of breast cancer cells[6–8]. We previously reported that CHIP levels were much higher in MCF-7 cells, a non-aggressive cell line derived from human breast cancer cells, than in MDA-MB-231 cells, a highly aggressive cell line. Furthermore, CHIP levels are negatively correlated with the malignancy of human breast tumor tissues[9]. In addition, CHIP suppresses both tumor growth and metastasis in a nude mouse xenograft model. Thus, it has been suggested that the regulation of CHIP expression may represent a potential new clinical approach to TNBC therapy.